



## Research paper



# Design and development of a new 4 DOF hybrid robot with Scara motion for high-speed operations in large workspace

Wen-ao Cao, Shiwei Li, Peng Cheng\*, Mingfeng Ge, Huafeng Ding, Jingpei Lai

School of Mechanical Engineering and Electronic Information, China University of Geosciences (Wuhan), 430074, Wuhan, China

## ARTICLE INFO

**Keywords:**  
Hybrid robot  
Mechanism design  
Kinematics  
Workspace  
Scara motion

## ABSTRACT

This paper presents a novel four-degree-of-freedom (4-DOF) hybrid robot named Hybrid-Long-Scara robot, which has the advantages of large workspace and low inertia. First, the kinematic mechanism of the new robot is designed based on requirements of its DOFs and actuation joints. Second, the closed-form displacement and velocity models of the new robot are established. Third, the workspace of the Hybrid-Long-Scara robot is quantitatively analyzed and the advantages of the new robot are visually shown. At last, a physical prototype is developed to verify the effectiveness of the mechanical design and kinematic model of the Hybrid-Long-Scara robot. Comparing with a typical Scara robot, the new robot can obtain larger vertical workspace based on a compact structure. On the other hand, comparing with a typical palletizing robot, the new robot can obtain higher motion speed, has a more compact height dimension, and can applied to wider operation tasks. With those characteristics, the Hybrid-Long-Scara robot has a good application prospect in high-speed sorting, grabbing, unstacking and packing in large workspace.

## 1. Introduction

Serial robots and parallel robots are two main categories of typical robots used in industries [1]. Generally, a multi-DOF serial robot has the advantages of large workspace and high dexterity. However, such a robot is difficult to apply to high-speed operations because of its large inertia brought by its actuation systems. Parallel robots have high speed and high stiffness [2-6], but suffer from the disadvantage of small workspace. Hybrid robots can be seen as the combination of serial robots and parallel robots, and have advantages of large workspace and low inertia [7,8].

Hybrid robots have a broad application prospect in aerospace manufacturing, and in assembly and packaging[9]. Many hybrid robots have been developed in the past several decades. The well-known Tricept robot has a hybrid structure with a 3-DOF parallel mechanism and a 2-DOF serial mechanism [10]. Romdhane [11] designed a 6-DOF hybrid manipulator which consisted of two parallel robots in series. Tsai and Joshi [12] proposed a hybrid mechanism which consisted of a position parallel mechanism and an orientation parallel mechanism. Huang et al. [13] proposed a reconfigurable hybrid robot for machining applications. Liang and Ceccarelli [14] designed a hybrid waist-trunk system consisted of a three-legged parallel mechanism and a six-legged parallel mechanism. Zhao et al. [15] studied kinematic calibration of a 6-DOF polishing Hybrid robot. Wang et al. [16] dealt with dynamics evaluation of a 5-DOF hybrid robot considering gravity. Wu et al. [17] proposed a hybrid 5-DOF robot composed of a delta parallel robot and a 2-DOF serial mechanism. Li et al. [18] studied the multi-objective optimization of dimensional synthesis for a 5-DOF hybrid robot. Huang et al.

\* Corresponding author.

E-mail address: [chengp@cug.edu.cn](mailto:chengp@cug.edu.cn) (P. Cheng).

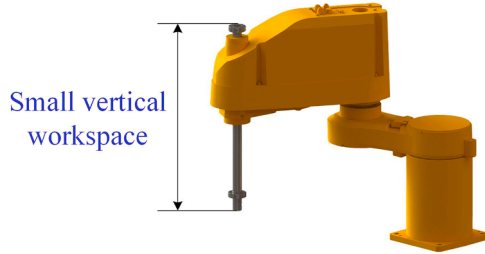


Fig. 1. A typical Scara robot.

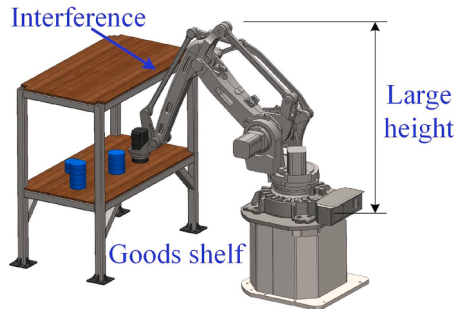


Fig. 2. A typical palletizing robot.

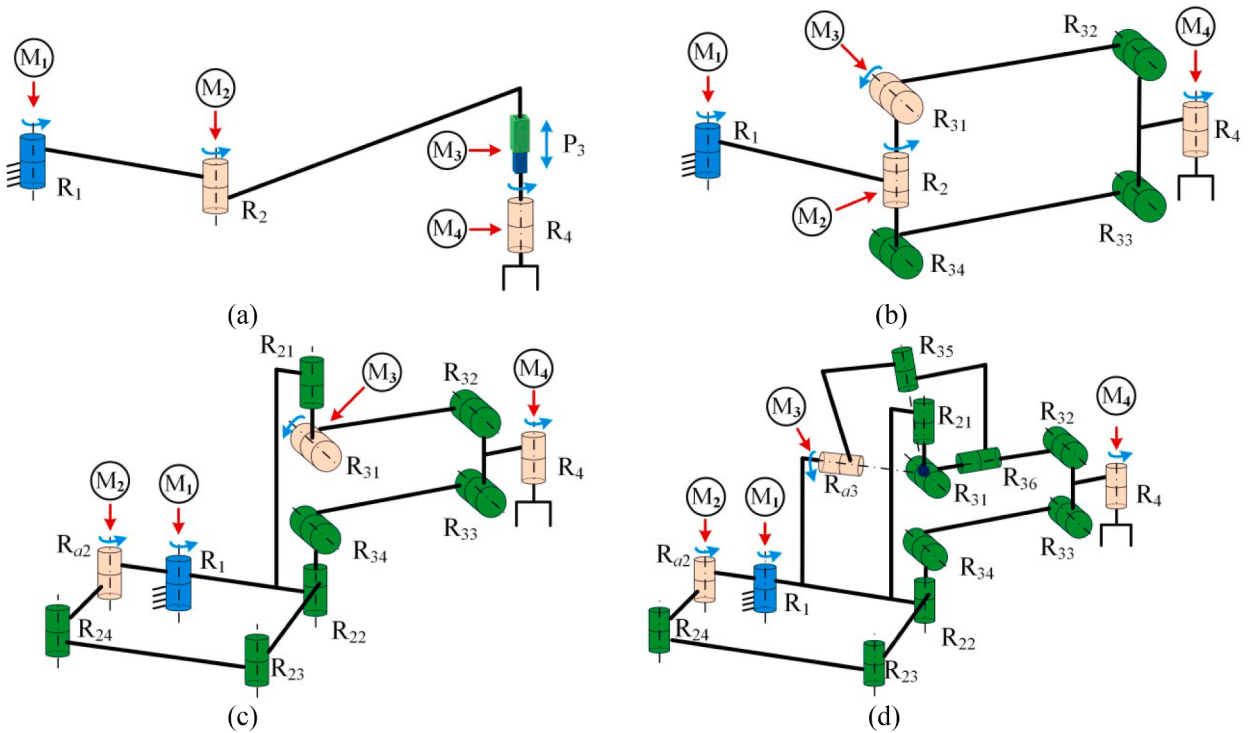


Fig. 3. Mechanical design derivation of the Hybrid-Long-Scara robot.

[19] established the dynamic model of a novel 5-DOF hybrid robot for machining. Qi et al. [20] performed stability analysis and distortion compensation of a hybrid robot simulator. Tao et al. [21] studied the kinematics and workspace of a 4-DOF hybrid palletizing robot. Zhao et al. [22] established the kinematics model of a hybrid mechanism based on recursive and inductive methods. Yu et al. [23] proposed a frequency response analysis of a heavy-load palletizing robot considering elastic deformation. Hu et al. [8,24]

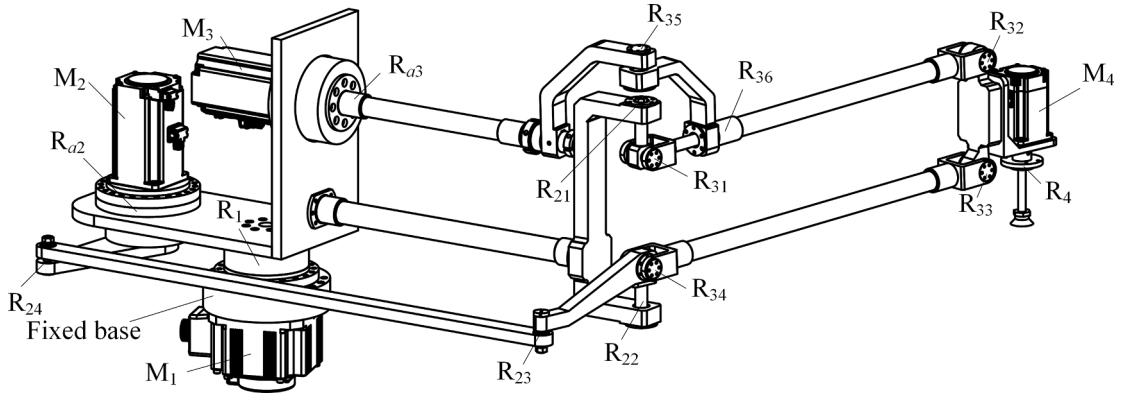


Fig. 4. Mechanical model of the Hybrid-Long-Scara robot.

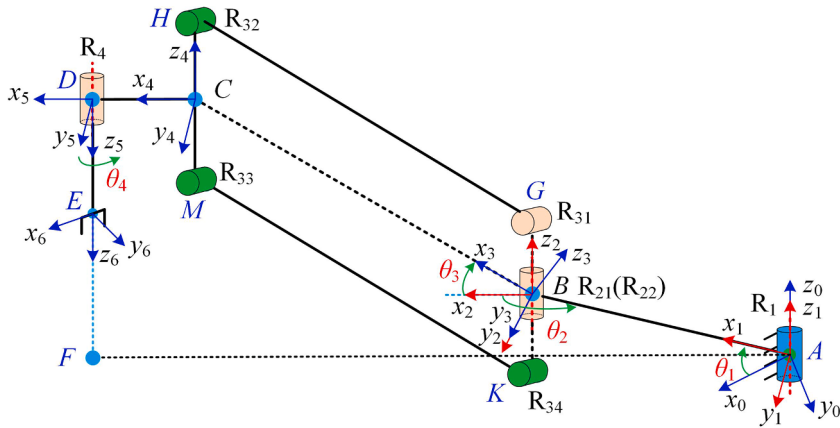


Fig. 5. Coordinate frames of the main kinematic mechanism.

studied the displacement of hybrid mechanisms based on elimination and conformal geometric algebra methods. Wang et al. [25] designed a control system of 4-DOF palletizing robot based on improved control multi-objective trajectory planning.

A robot with Scara motion (three translations and one rotation) has been widely applied to pick and place, grabbing, handling, stacking and unstacking operations. A typical Scara serial robot can obtain high speed but it has small vertical workspace, as shown in Fig. 1. A typical 4-DOF palletizing robot is a hybrid robot which can produce Scara motion [21], but such a robot has the following main disadvantages: (1) It is difficult to realize high-speed operations because large torques brought by own weight needs to be undertaken by its actuators. (2) It is difficult to operate inside a goods shelf because interference occurs easily between the robot and the shelf, as shown in Fig. 2. (3) The robot needs to occupy great installation space along the vertical direction because it has a large own height.

In this paper, a novel 4-DOF hybrid robot with Scara motion is presented, which has large vertical and horizontal workspace with relatively low own height, and can realize operation tasks inside a goods shelf. The remainder of this paper is organized as follows. Section 2, the kinematic mechanism of the new hybrid robot is designed. In Section 3, the displacement and velocity model of the new robot are established. In Section 4, the workspace of the robot is analyzed. In Section 5, a physical prototype of the robot is developed. In Section 6, some discussions of the new robot are presented. Finally, some conclusions of this work are drawn in Section 7.

## 2. Mechanical design of the Hybrid-Long-Scara robot

The new robot is expected to satisfy the following design requirements: (1) output Scara motion for pick and place applications, (2) only have revolute pairs for higher dexterity and less wear, and (3) most actuators are located at the base or near the base to obtain high-speed motion. Based on those requirements, the corresponding kinematic mechanism can be performed for the new robot as follows.

Firstly, a typical mechanism corresponding to design requirement 1 is shown in Fig. 3(a), which includes three parallel revolute pairs ( $R_1$ ,  $R_2$  and  $R_4$ ) and one prismatic pair ( $P_3$ ), and four motors located at the four pairs.

Secondly, to satisfy design requirement 2, a parallelogram linkage is used to replace  $P_3$  of the mechanism in Fig. 3(a). Then, a new mechanism is obtained, shown in Fig. 3(b).

Thirdly, to satisfy design requirement 3,  $R_2$  is replaced by two coaxial  $R_{21}$  and  $R_{22}$ , and a parallelogram linkage consisting of  $R_{a2}$ ,  $R_{24}$ ,  $R_{23}$  and  $R_{22}$  is introduced into the mechanism in Fig. 3(b). Then, a new mechanism is shown in Fig. 3(c), in which  $R_{a2}$ ,  $R_{24}$ ,  $R_{23}$  and  $R_{22}$  are parallel to each other. In this way, motor 2 ( $M_2$ ) can be transferred to  $R_{a2}$  close to the base.

Lastly, a spherical four-linkage including  $R_{a3}$ ,  $R_{35}$ ,  $R_{36}$  and  $R_{31}$  is introduced to the mechanism in Fig. 3(c), and a new mechanism is shown in Fig. 3(d), in which  $R_{a3}$ ,  $R_{35}$ ,  $R_{36}$ ,  $R_{31}$  and  $R_{21}$  are concurrent at the geometrical center of  $R_{31}$ . In this way, motor 3 ( $M_3$ ) can be also transferred to  $R_{a3}$  close to the base.

Because the introduced 3R planar chain ( $R_{a2}$ ,  $R_{24}$  and  $R_{23}$ ) and the 3R spherical chain ( $R_{a3}$ ,  $R_{35}$  and  $R_{36}$ ) cannot influence the DOF, the mechanism shown in Fig. 3(d) can output the same Scara motion as the mechanism shown in Fig. 3(b). Based on the mechanism shown in Fig. 3(d), the whole mechanical model of the Hybrid-Long-Scara robot can be constructed, as shown in Fig. 4.

### 3. Displacement and velocity analysis of the Hybrid-Long-Scara robot

Based on the above design, the mechanism in Fig. 3(b) is the main kinematic mechanism of the hybrid robot. Some coordinate frames are needed to be attached for kinematics analysis, as shown in Fig. 5. Fixed frame 0 can be attached to the geometrical center A of  $R_1$  on the base platform, with  $x_0$  axis pointing to link AB,  $z_0$  axis along the axis of  $R_1$ , and  $y_0$  determined by the right-hand rule. Moving frame 6 can be attached to the geometrical center E of the end effector, with  $x_6$  along the opening and closing direction of the end effector,  $z_6$  axis along the axis of  $R_4$ , and  $y_6$  determined by the right-hand rule. In this figure, point F is the projection of point E onto  $x_0y_0$  plane.

The orientation of the end effector can be represented by a rotation matrix about its  $z$  axis by angle,

$$\mathbf{R}_e = \begin{pmatrix} \cos\gamma & -\sin\gamma & 0 \\ \sin\gamma & \cos\gamma & 0 \\ 0 & 0 & 1 \end{pmatrix} \quad (1)$$

The position of the end effector can be expressed as

$$\mathbf{r}_e = (X_e \ Y_e \ Z_e)^T \quad (2)$$

where  $X_e$ ,  $Y_e$ , and  $Z_e$  represent  $x$ ,  $y$  and  $z$  components of the vector, respectively, and the superscript  $T$  represents the transpose operation.

For the following displacement analysis, several middle frames are needed to be set up. Frame 1 is attached to central point B of  $R_2$ , with  $x_1$  axis pointing to link AB,  $z_1$  axis along the axis of  $R_1$ . Frame 2 is attached to central point B of  $R_{21}$ , with  $z_2$  axis along the axis of  $R_{21}$ , and with  $x_2$  along the projection of line BC onto  $x_0y_0$  plane. Frame 3 is also attached to central point B of  $R_{21}$ , with  $z_3$  parallel to the axis of  $R_{31}$ , and  $x_3$  along line BC. Frame 4 is attached to point C, with  $x_4$  axis along link CD,  $z_4$  axis along link MH. Frame 5 is attached to central point D of  $R_4$ , with  $x_5$  axis parallel to  $x_6$  axis,  $z_5$  axis along the axis of  $R_4$ .

#### 3.1. Direct displacement analysis of the new robot

From Fig. 5, the homogeneous transformation of the end-effector can be expressed as

$${}_1^0\mathbf{T} {}_2^1\mathbf{T} {}_3^2\mathbf{T} {}_4^3\mathbf{T} {}_5^4\mathbf{T} {}_6^5\mathbf{T} = {}_6^0\mathbf{T} = \begin{pmatrix} \mathbf{R}_e & \mathbf{r}_e \\ \mathbf{0} & 1 \end{pmatrix} \quad (3)$$

where

$$\left\{ \begin{array}{l} {}_1^0\mathbf{T} = \begin{pmatrix} {}_0^1\mathbf{R} & \mathbf{p}_1 \\ 0 & 1 \end{pmatrix} = \begin{pmatrix} c\theta_2 & -s\theta_2 & 0 & 0 \\ s\theta_2 & c\theta_2 & 0 & 0 \\ 0 & 0 & 0 & 0 \\ 0 & 0 & 0 & 1 \end{pmatrix}, {}_2^1\mathbf{T} = \begin{pmatrix} {}_1^2\mathbf{R} & \mathbf{p}_2 \\ 0 & 1 \end{pmatrix} = \begin{pmatrix} c\theta_2 & -s\theta_2 & 0 & L_{AB} \\ s\theta_2 & c\theta_2 & 0 & 0 \\ 0 & 0 & 0 & 0 \\ 0 & 0 & 0 & 1 \end{pmatrix}, \\ {}_3^2\mathbf{T} = \begin{pmatrix} {}_2^3\mathbf{R} & \mathbf{p}_3 \\ 0 & 1 \end{pmatrix} = \begin{pmatrix} c\theta_3 & 0 & s\theta_3 & 0 \\ 0 & 1 & 0 & 0 \\ -s\theta_3 & 0 & c\theta_3 & 0 \\ 0 & 0 & 0 & 1 \end{pmatrix}, {}_4^3\mathbf{T} = \begin{pmatrix} -{}_2^3\mathbf{R} & \mathbf{p}_4 \\ 0 & 1 \end{pmatrix} = \begin{pmatrix} -c\theta_3 & 0 & -s\theta_3 & L_{BC} \\ 0 & 1 & 0 & 0 \\ s\theta_3 & 0 & -c\theta_3 & 0 \\ 0 & 0 & 0 & 1 \end{pmatrix} \end{array} \right. \quad (4)$$

and

$${}_5^4\mathbf{T} = \begin{pmatrix} {}_4^5\mathbf{R} & \mathbf{p}_4 \\ 0 & 1 \end{pmatrix} = \begin{pmatrix} 1 & 0 & 0 & L_{CD} \\ 0 & 1 & 0 & 0 \\ 0 & 0 & 1 & 0 \\ 0 & 0 & 0 & 1 \end{pmatrix}, {}_6^5\mathbf{T} = \begin{pmatrix} {}_5^6\mathbf{R} & \mathbf{p}_5 \\ 0 & 1 \end{pmatrix} = \begin{pmatrix} c\theta_4 & -s\theta_4 & 0 & L_{DE} \\ s\theta_4 & c\theta_4 & 0 & 0 \\ 0 & 0 & 1 & 0 \\ 0 & 0 & 0 & 1 \end{pmatrix} \quad (5)$$

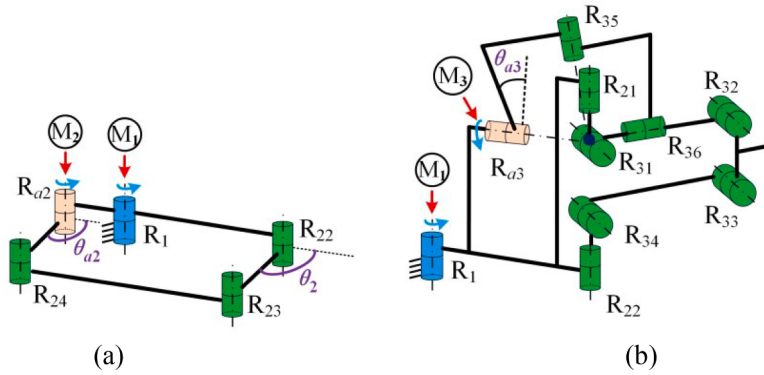


**Fig. 6.** Actuation linkages of the Hybrid-Long-Scara robot.

in which  $c\#$  and  $s\#$  represent  $\cos(\#)$  and  $\sin(\#)$ , respectively,  $\theta_i$  is the joint angle of  $R_i$ , and  $L_{XY}$  denotes the link length determined by points  $X$  and  $Y$ .

Based on the design process of Fig. 3, for the parallelogram actuation linkage shown in Fig. 6(a), it can be easily obtained,

$$\theta_{a2} = \theta_2 \quad (6)$$

where  $\theta_{a2}$  is the actuation angle transferred by pair  $R_2$ .

For the actuation linkage shown in Fig. 6(b), pairs  $R_{a3}$  and  $R_{35}$  are perpendicular to each other, and pairs  $R_{35}$  and  $R_{36}$  are perpendicular to each other. With respect to frame 1, the axis of pair  $R_{31}$  can be expressed as

$${}^1S_{35} = (0 \quad \cos\theta_{a3} \quad \sin\theta_{a3})^T \quad (7)$$

where  $\theta_{a3}$  is the actuation angle transferred by pair  $R_3$ .

The axis direction of  $R_{36}$  is along link  $GH$ , and the direction with respect to frame 1 can be expressed as

$${}^1S_{36} = (\cos\theta_2 \cos\theta_3 \quad \cos\theta_3 \sin\theta_2 \quad -\sin\theta_3)^T \quad (8)$$

Based on the perpendicular relation between  ${}^1S_{35}$  and  ${}^1S_{36}$ , the dot product of them is

$$\cos\theta_{a1}\cos\theta_3\sin\theta_2 - \sin\theta_{a1}\sin\theta_3 = 0 \quad (9)$$

Then,

$$\theta_3 = \arctan\left(\frac{\sin\theta_2}{\tan\theta_{a1}}\right) \quad (10)$$

From Eqs. (3), (6) and (10), when four actuation angles  $\theta_1$ ,  $\theta_{a2}$ ,  $\theta_{a3}$  and  $\theta_4$  are given, the position and orientation of the end effector of the robot can be determined. Therefore, the direct position analysis has been finished.

### 3.2. Inverse displacement analysis of the new robot

From Fig. 5, the closed-loop vector equation can be set as

$$\mathbf{r}_e = L_{AB}\mathbf{u}_{AB} + L_{BC}\mathbf{u}_{BC} + L_{CD}\mathbf{u}_{CD} + L_{DE}\mathbf{u}_{DE} \quad (11)$$

where  $\mathbf{u}_{XY}$  denotes the direction of link  $XY$ , and

$$\begin{cases} \mathbf{u}_{AB} = (\cos\theta_1 \quad \sin\theta_1 \quad 0)^T; \mathbf{u}_{DE} = (0 \quad 0 \quad 1)^T \\ \mathbf{u}_{BC} = (\cos\theta_3(\cos\theta_1\cos\theta_2 - \sin\theta_1\sin\theta_2) \quad \cos\theta_3(\cos\theta_1\sin\theta_2 + \cos\theta_2\sin\theta_1) \quad \sin\theta_3)^T \\ \mathbf{u}_{CD} = (\cos\theta_1\cos\theta_2 - \sin\theta_1\sin\theta_2 \quad \cos\theta_1\sin\theta_2 + \cos\theta_2\sin\theta_1 \quad 0)^T \end{cases} \quad (12)$$

From Eqs. (11) and (12), it can be obtained,

$$\sin\theta_3 = \frac{z_p - L_{DE}}{L_{BC}} \quad (13)$$

From the structure of the robot,  $\theta_3$  is from  $-\pi/2$  to  $\pi/2$ , so,

$$\theta_3 = \arcsin\left(\frac{z_p - L_{DE}}{L_{BC}}\right) \quad (14)$$

Shown in Fig. 5, the position of projection point  $F$  of point  $E$  onto the  $x_0y_0$  plane of fixed frame 0 is

$$\mathbf{r}_F = (x_e \quad y_e \quad 0)^T \quad (15)$$

In the triangular  $ABF$ , there exists

$$\begin{cases} L_{BF} = L_{CD} + L_{BC}\cos\theta_3 \\ L_{AF} = |\mathbf{r}_F| \end{cases} \quad (16)$$

According to the law of cosines, the following equation can be obtained,

$$\cos\theta_2 = \frac{(L_{AB})^2 + (L_{BF})^2 - (L_{AF})^2}{2L_{AB}L_{BF}} \quad (17)$$

Then,

$$\theta_2 = \arccos \frac{(L_{AB})^2 + (L_{BF})^2 - (L_{AF})^2}{2L_{AB}L_{BF}} \quad (18)$$

Substituting Eqs. (14) and (18) into Eq. (11), then

$$\begin{cases} M_1\cos\theta_1 + N_1\sin\theta_1 = x_e \\ M_2\cos\theta_1 + N_2\sin\theta_1 = y_e \end{cases} \quad (19)$$

where

$$\begin{cases} M_1 = (L_{CD} + L_{BC}\cos\theta_3)\cos\theta_2 + L_{AB}; N_1 = (L_{CD} + L_{BC}\cos\theta_3)\sin\theta_2 \\ M_2 = (L_{CD} + L_{BC}\cos\theta_3)\sin\theta_2; N_2 = -(L_{CD} + L_{BC}\cos\theta_3)\cos\theta_2 - L_{AB} \end{cases} \quad (20)$$

Then,

$$\cos\theta_1 = \frac{x_eN_2 - y_eN_1}{M_1N_2 - M_2N_1}; \sin\theta_1 = \frac{x_eM_2 - y_eM_1}{N_1M_2 - N_2M_1} \quad (21)$$

Hence,

$$\theta_1 = \text{atan2}(\sin\theta_1, \cos\theta_1) \quad (22)$$

From Eq.(3), the orientation matrix of the robot satisfies

$${}_1\mathbf{R}_2^1\mathbf{R}_3^2\mathbf{R}_4^3\mathbf{R}_5^4\mathbf{R}_6^5\mathbf{R} = \mathbf{R}_e \quad (23)$$

Combining Eq. (23) with Eq. (4), yields

$$\begin{pmatrix} c\theta_4c(\theta_1 + \theta_2) - s\theta_4s(\theta_1 + \theta_2) & -c\theta_4s(\theta_2 - \theta_1) - s\theta_4c(\theta_1 - \theta_2) & 0 \\ c\theta_4s(\theta_1 + \theta_2) + s\theta_4c(\theta_1 + \theta_2) & c\theta_4c(\theta_1 - \theta_2) - s\theta_4s(\theta_2 - \theta_1) & 0 \\ 0 & 0 & 1 \end{pmatrix} = \begin{pmatrix} c\gamma & -s\gamma & 0 \\ s\gamma & c\gamma & 0 \\ 0 & 0 & 1 \end{pmatrix} \quad (24)$$

Entries (1,1) and (2,1) of two sides of Eq. (24) are correspondingly equal, therefore,

$$\begin{cases} M_3\cos\theta_4 + N_3\sin\theta_4 = \cos\gamma \\ M_4\cos\theta_4 + N_4\sin\theta_4 = \sin\gamma \end{cases} \quad (25)$$

where

$$M_3 = \cos(\theta_2 - \theta_1); N_3 = -\sin(\theta_2 - \theta_1); M_4 = \sin(\theta_2 - \theta_1); N_4 = \cos(\theta_2 - \theta_1) \quad (26)$$

Then,

$$\cos\theta_4 = \frac{\cos\gamma N_2 - \sin\gamma N_1}{M_1N_2 - M_2N_1}, \sin\theta_4 = \frac{\cos\gamma M_2 - \sin\gamma M_1}{N_1M_2 - N_2M_1} \quad (27)$$

Hence

$$\theta_4 = \text{atan2}(\sin\theta_4, \cos\theta_4) \quad (28)$$

From Eq.(6)

$$\theta_{a2} = \theta_2 \quad (29)$$

From Eq.(9)

$$\theta_{a3} = \arctan\left(\frac{\sin\theta_2}{\tan\theta_3}\right) \quad (30)$$

From Eqs. (14), (18), (22), (28), (29) and (30), when the position and orientation of the end effector of the robot are given, four actuation angles  $\theta_1$ ,  $\theta_{a2}$ ,  $\theta_{a3}$  and  $\theta_4$  can be determined. Therefore, the inverse position analysis of the robot has been finished.

### 3.3. Velocity model of the new robot

Taking the derivative of two sides of Eq. (11), yields

$$\nu = \dot{\theta}_1 S_1 \times L_{AB} \mathbf{u}_{AB} + (\dot{\theta}_1 S_1 + \dot{\theta}_2 S_2 + \dot{\theta}_3 S_3) \times L_{BC} \mathbf{u}_{BC} + (\dot{\theta}_1 S_1 + \dot{\theta}_2 S_2) \times L_{CD} \mathbf{u}_{CD} \quad (31)$$

where

$$S_1 = S_2 = (0 \ 0 \ 1)^T, S_3 = (\cos\theta_1 \cos\theta_2 - \sin\theta_1 \sin\theta_2 \ \cos\theta_1 \sin\theta_2 + \cos\theta_2 \sin\theta_1 \ 0)^T \quad (32)$$

Dot multiplying both sides of Eq. (31) with  $\mathbf{u}_{BC}$ , yields

$$\mathbf{u}_{BC} \cdot \nu = (\dot{\theta}_1 S_1 \times L_{AB} \mathbf{u}_{AB}) \cdot \mathbf{u}_{BC} \quad (33)$$

Then,

$$\dot{\theta}_1 = J_1 \nu \quad (34)$$

where

$$J_1 = \frac{(\mathbf{u}_{BC})^T}{(S_1 \times L_{AB} \mathbf{u}_{AB})(\mathbf{u}_{BC})^T} \quad (35)$$

Dot multiplying both sides of Eq. (31) with  $S_3$ , yields

$$S_3 \cdot \nu = \dot{\theta}_1 S_1 \times L_{AB} \mathbf{u}_{AB} \cdot S_3 + (\dot{\theta}_1 S_1 + \dot{\theta}_2 S_2) \times L_{BC} \mathbf{u}_{BC} \cdot S_3 + (\dot{\theta}_1 S_1 + \dot{\theta}_2 S_2) \times L_{CD} \mathbf{u}_{CD} \cdot S_3 \quad (36)$$

Combing Eqs.(36) with Eq. (34), yields

$$\dot{\theta}_2 = J_2 \nu \quad (37)$$

where

$$J_2 = \frac{(S_3)^T - S_1 \times (L_{AB} \mathbf{u}_{AB} + L_{BC} \mathbf{u}_{BC} + L_{CD} \mathbf{u}_{CD}) \cdot S_3 \cdot J_1}{S_1 \times (L_{BC} \mathbf{u}_{BC} + L_{CD} \mathbf{u}_{CD}) \cdot S_3} \quad (38)$$

Dot multiplying both sides of Eq. (31) with  $S_1$ , yields

$$S_1 \cdot \nu = \dot{\theta}_3 S_3 \times L_{BC} \mathbf{u}_{BC} \cdot S_1 \quad (39)$$

Then

$$\dot{\theta}_3 = J_3 \nu \quad (40)$$

where

$$J_3 = \frac{(S_1)^T}{S_3 \times L_{BC} \mathbf{u}_{BC} \cdot S_1} \quad (41)$$

End angular velocity  $\omega$  of the robot can be expressed as

$$\dot{\theta}_1 S_1 + \dot{\theta}_2 S_2 + \dot{\theta}_4 S_4 = \omega \quad (42)$$

where

$$S_4 = S_1 = S_2 = (0 \ 0 \ 1)^T \quad (43)$$

Then

$$\dot{\theta}_4 = S_4 \cdot \omega - \dot{\theta}_1 - \dot{\theta}_2 \quad (44)$$

Substituting Eqs. (34) and (37) into Eq. (42), yields

$$\dot{\theta}_4 = J_4 \begin{pmatrix} \nu \\ \omega \end{pmatrix} \quad (45)$$

where

**Table 1**

Main link dimensions.

$L_{AB}(\text{mm})$	$L_{GH}(\text{mm})$	$L_{HM}(\text{mm})$	$L_{CD}(\text{mm})$	$L_{DE}(\text{mm})$
600	600	150	90	50

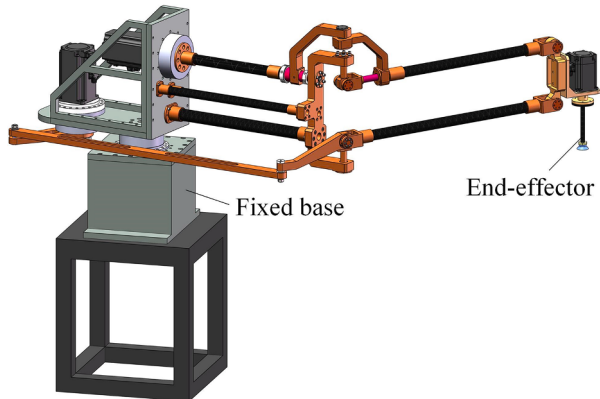


Fig. 7. The three-dimensional model of the new robot.

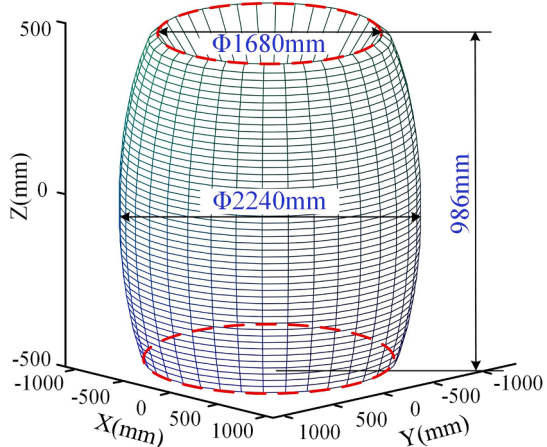


Fig. 8. The workspace of the new robot.

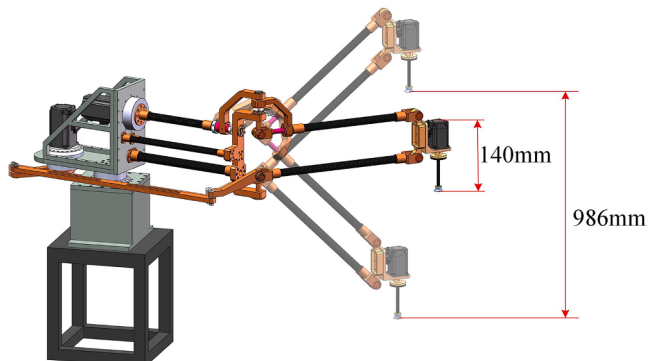
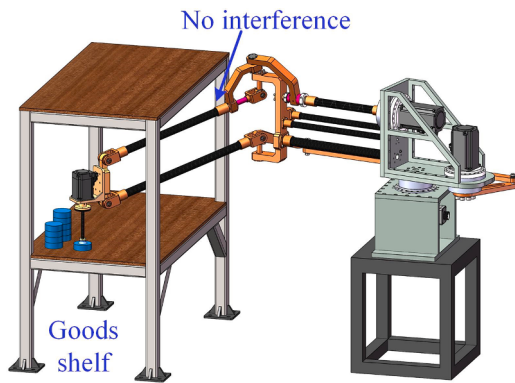
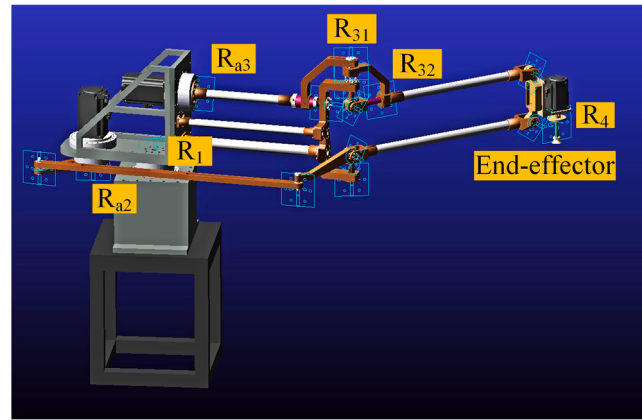


Fig. 9. The vertical workspace of the new robot.



**Fig. 10.** Operations of the new robot inside a shelf.



**Fig. 11.** The virtual prototype of the new robot.

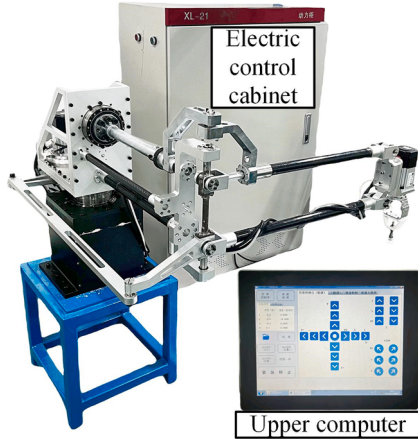


**Fig. 12.** The physical prototype of the new robot.

$$\mathbf{J}_4 = (-\mathbf{J}_1 - \mathbf{J}_2 \quad (\mathbf{S}_1)^T) \quad (46)$$

From Eq. (29)

$$\dot{\theta}_{a2} = \dot{\theta}_2 = \mathbf{J}_{a2}\mathbf{v} \quad (47)$$

where

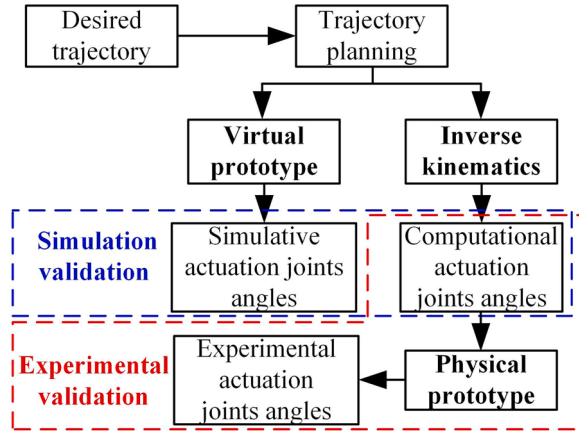


Fig. 13. Flowchart of the verification of the new robot.

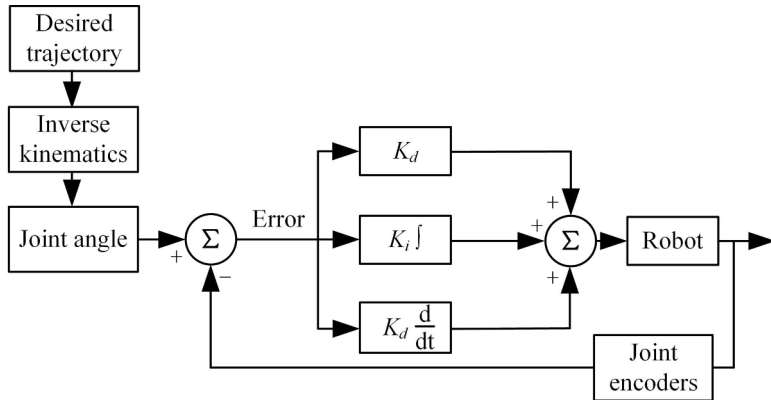


Fig. 14. PID position control scheme of the robot.

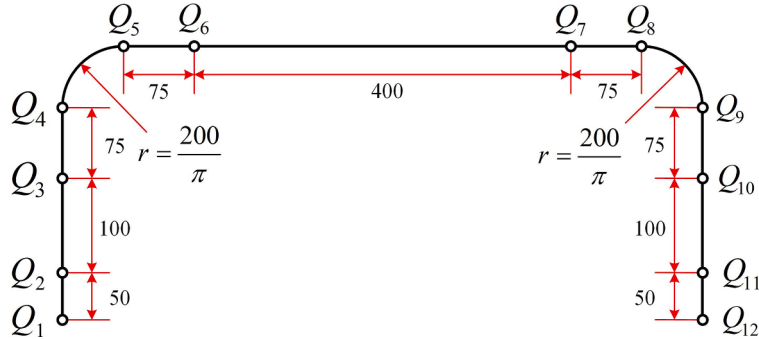


Fig. 15. A typical gate path for a pick-and-place operation.

$$J_{a2} = J_2 \quad (48)$$

From Eq. (30)

$$\dot{\theta}_{a3} = \frac{\dot{\theta}_3 \sec^2 \theta_3 \sin \theta_2 - \dot{\theta}_2 \tan \theta_3 \cos \theta_2}{\sin^2 \theta_2 + \tan^2 \theta_3} \quad (49)$$

Then

$$\dot{\theta}_{a3} = J_{a3} v \quad (50)$$

**Table 2**  
Trajectories of all sub-paths.

Subpaths	Time	Motion states	Trajectories
$Q_1-Q_2$	$T_1=T/16, 0 \leq t \leq T_1$	Acceleration	$x_p = -600, y_p = 600, z_p = 75 + 200t - \frac{50}{\pi} \sin(4\pi t)$
$Q_2-Q_3$	$T_2=T/16, T_1 \leq t \leq T_2$	Uniform	$x_p = -600, y_p = 600, z_p = 25 + 400t$
$Q_3-Q_4$	$T_3=T/16,$ $T_2 \leq t \leq T_3$	Deceleration	$x_p = -600, y_p = 600, z_p = 75 + 300t + \frac{25}{\pi} \sin(4\pi(t - 0.5))$
$Q_4-Q_5$	$T_4=T/8,$ $T_3 \leq t \leq T_4$	Uniform	$x_p = -600 + \frac{200}{\pi}(1 - \cos(\pi(t - 0.75))), y_p = 600; z_p = 300 + \frac{200}{\pi} \sin(\pi(t - 0.75))$
$Q_5-Q_6$	$T_5=T/16,$ $T_4 \leq t \leq T_5$	Acceleration	$x_p = \frac{-25}{\pi} (\sin(4\pi(t - 1.25)) + 39\pi - 12\pi t - 8); y_p = 600; z_p = 300 + \frac{200}{\pi}$
$Q_6-Q_7$	$T_6=T/4,$ $T_5 \leq t \leq T_6$	Uniform	$x_p = -525 + \frac{200}{\pi} + 400(t - 1.5), y_p = 600; z_p = 300 + \frac{200}{\pi}$
$Q_7-Q_8$	$T_7=T/16,$ $T_6 \leq t \leq T_7$	Deceleration	$x_p = \frac{25}{\pi} (\sin(4\pi(t - 2.5)) - 35\pi + 12\pi t + 8); y_p = 600; z_p = 300 + \frac{200}{\pi}$
$Q_8-Q_9$	$T_8=T/8,$ $T_7 \leq t \leq T_8$	Uniform	$x_p = \frac{50}{\pi} (4\sin(\pi(t - 2.75)) - \pi + 4); y_p = 600; z_p = \frac{100}{\pi} (3\pi + 2\cos(\pi(t - 2.75)))$
$Q_9-Q_{10}$	$T_9=T/16,$ $T_8 \leq t \leq T_9$	Acceleration	$x_p = -50 + \frac{400}{\pi}, y_p = 600; z_p = 300 - 300(t - 3.25) + \frac{25}{\pi} \sin(4\pi(t - 3.25))$
$Q_{10}-Q_{11}$	$T_{10}=T/16,$ $T_9 \leq t \leq T_{10}$	Uniform	$x_p = -50 + \frac{400}{\pi}, y_p = 600; z_p = 225 - 400(t - 3.5)$
$Q_{11}-Q_{12}$	$T_{11}=T/16,$ $T_{10} \leq t \leq T_{11}$	Deceleration	$x_p = -50 + \frac{400}{\pi}, y_p = 600; z_p = 125 - 200(t - 3.75) - \frac{50}{\pi} \sin(4\pi(t - 3.75))$

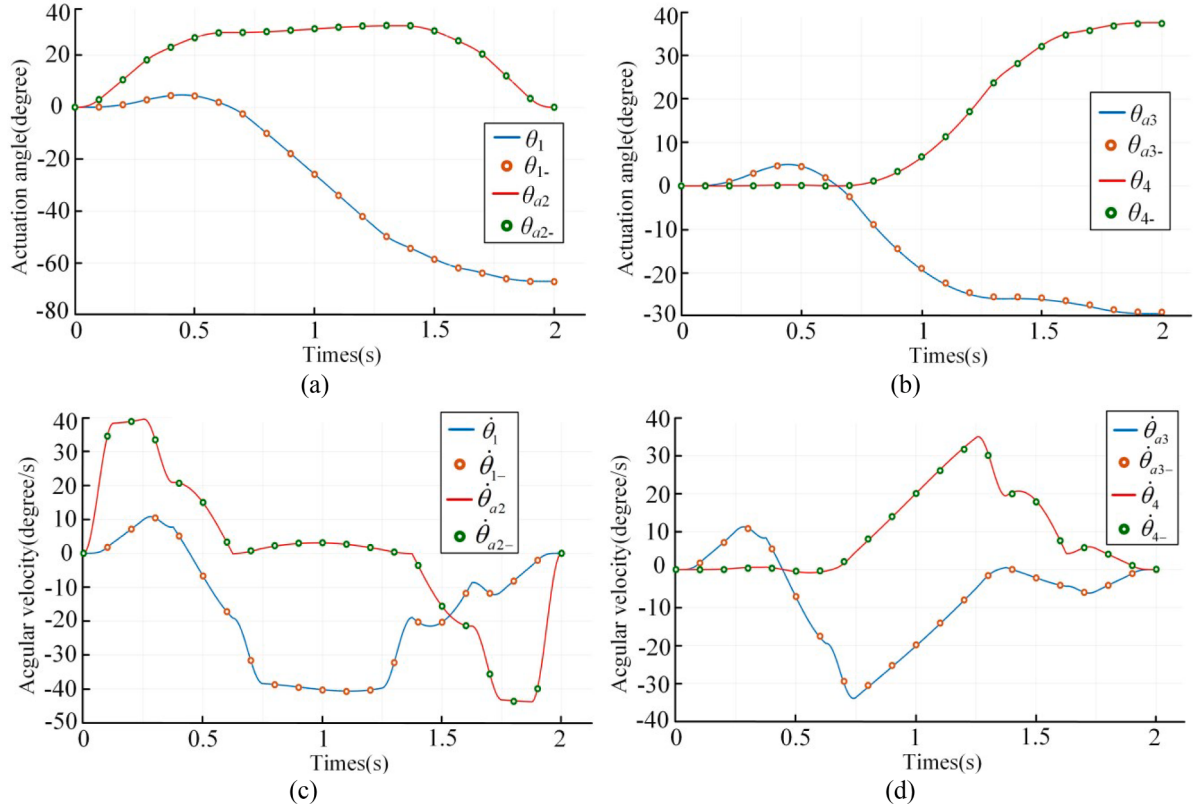


**Fig. 16.** Computational and simulative results of four actuation joints: (a) angles of actuation joints 1 and 2, (b) angles of actuation joints 3 and 4, (c) angular velocities of actuation joints 1 and 2, and (d) angular velocities of actuation joints 3 and 4.

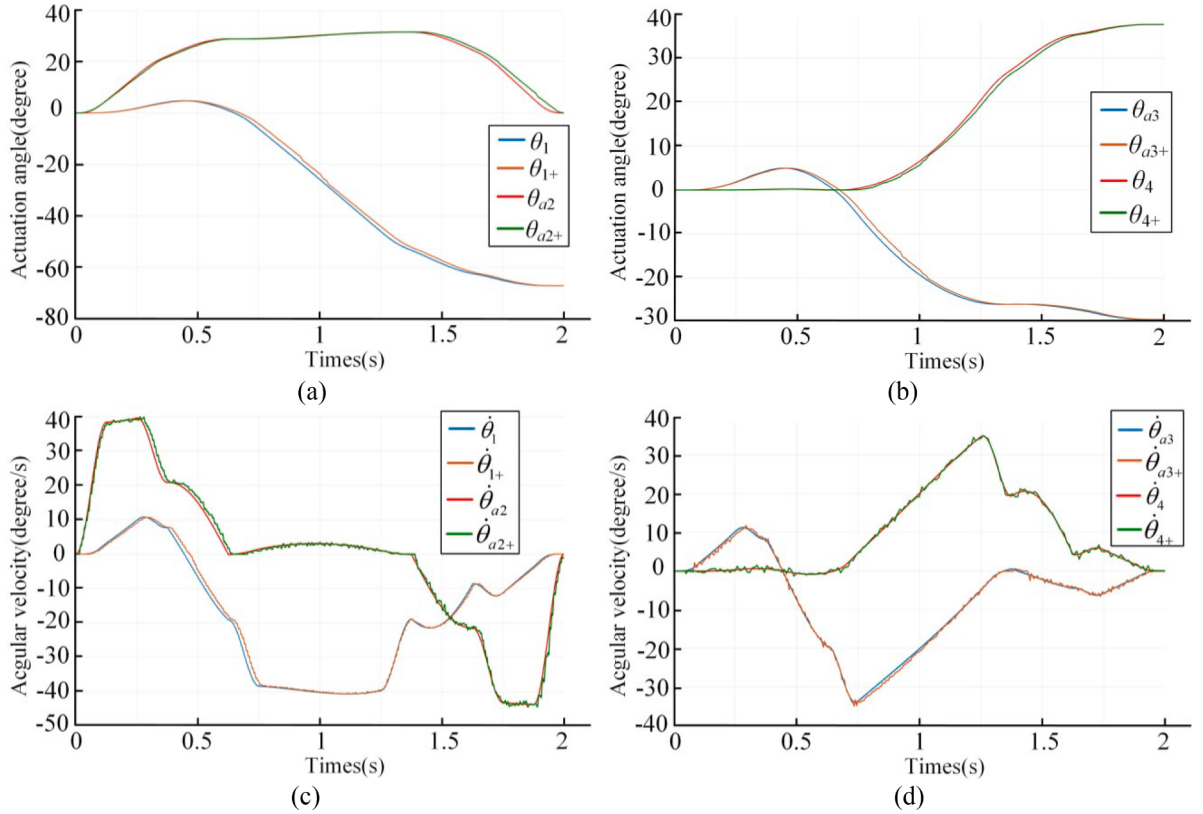


**Fig. 17.** Comparisons between computational results and experimental results of four actuation joints.

where

$$J_{a3} = \frac{J_3 \sec^2 \theta_3 \sin \theta_2 - J_2 \tan \theta_3 \cos \theta_2}{\sin^2 \theta_2 + \tan^2 \theta_3} \quad (51)$$

From Eqs. (34), (45), (47) and (50), it can be obtained,

$$(\dot{\theta}_1 \quad \dot{\theta}_{2a} \quad \dot{\theta}_{3a} \quad \dot{\theta}_4)^T = J \begin{pmatrix} v \\ \omega \end{pmatrix} \quad (52)$$

where

$$J = \begin{pmatrix} J_1 & \mathbf{0} \\ J_{a2} & \mathbf{0} \\ J_{a3} & \mathbf{0} \\ -J_1 - J_2 & (S_1)^T \end{pmatrix} \quad (53)$$

which can be called the kinematics Jacobian matrix of the hybrid robot.

#### 4. Workspace analysis of the Hybrid-Long-Scara robot

Here, take constructing cylindrical workspace with a diameter of about 2 m for example. In this case, the sum of the lengths of links  $AB$  and  $GH$  is required to be greater than and close to 1 meter for the main kinematic mechanism shown in Fig. 5. Therefore, links  $AB$  and  $BC$  are first given as the length of 0.6 m, respectively. Other link dimensions are determined based on assembly requirement of joints and actuators. Finally, main link dimensions are given in Table 1.

Based on those dimensions, a three-dimensional model of the robot can be established shown in Fig. 7. Based on the model, ranges of joint angles and actuation angels can be described as

$$\begin{cases} 0^\circ \leq \theta_1 \leq 360^\circ; \\ 20^\circ \leq \theta_{21} = \theta_{22} = \theta_{a2} \leq 160^\circ; \\ -80^\circ \leq \theta_3 \leq 80^\circ; 20^\circ \leq \theta_{a3} \leq 160^\circ; 0^\circ \leq \theta_4 \leq 360^\circ \end{cases} \quad (54)$$

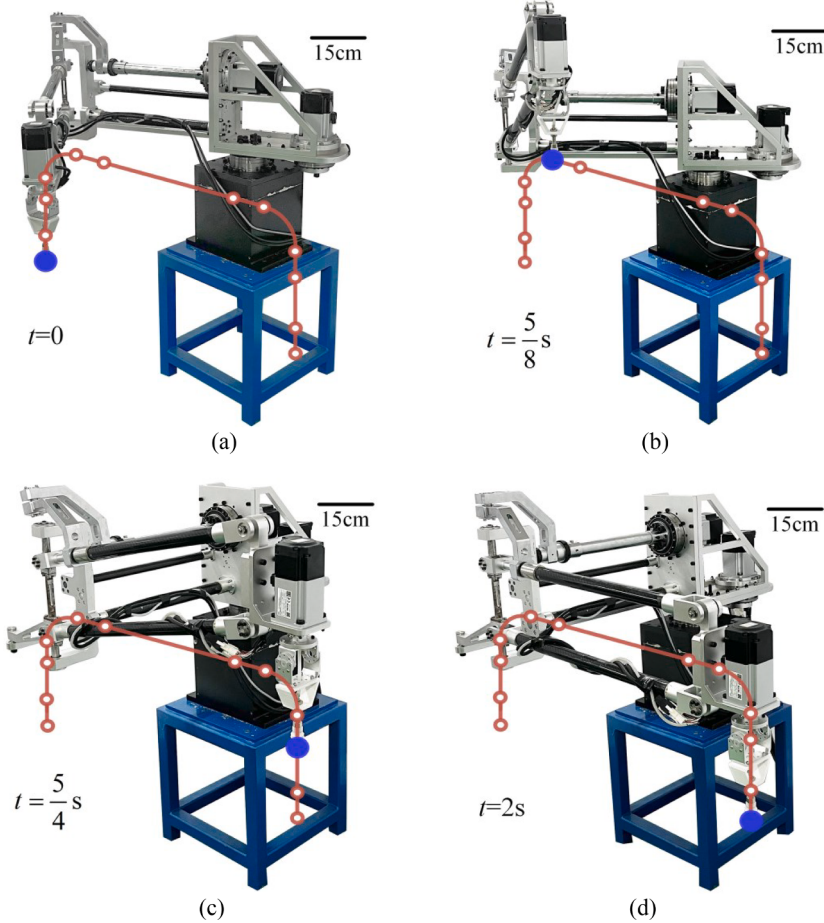


**Fig. 18.** End-effector positions of the new hybrid robot.

Under the link dimensions and angle ranges, the workspace of the new hybrid robot is shown in Fig. 8, with a height of close to 1 meter and a diameter of about 2 m.

From Fig. 9, it can be seen that movable members of the hybrid robot only have their own height of 0.14 m, but it can obtain vertical workspace with a height of about 1 meter. It illustrates the robot can obtain large workspace with a relatively small itself height. Hence, the robot needs to occupy relatively low vertical installation space. Besides, the hybrid robot can realize the piece-picking tasks inside a shelf, as shown in Fig. 10.

##### 5. Prototype development and experiment verification of the Hybrid-Long-Scara robot

Based on ADAMS commercial software, a virtual prototype of the Hybrid-Long-Scara robot can be established, shown in Fig. 11. Further, a physical prototype of the new hybrid robot has been developed, shown in Fig. 12, where most links and frames are made of lighter aluminum alloy, the slender links of the parallelogram mechanism are made of carbon fiber, and all motors are servo motors with absolute encoders. The verification of the Hybrid-Long-Scara robot can be divided into the simulation validation with comparisons between computational results and simulative results, and the experiment validation with the comparisons between computational results and experimental results, as shown in Fig. 13.

The new robot is expected to apply to the pick and place operations, for which kinematic control is enough to satisfy operation requirements. The PID position control strategy [26] is applied to the proposed robot and tuned to optimally control the positions of four actuators, with which the actual trajectory can achieve proximity to the desired trajectory. The PID algorithm comprises three parameters:  $K_p$ ,  $K_i$  and  $K_d$ , which denote the gain of the current joint angle error, integration of the error, and differential of the error, respectively, as shown in Fig. 14.

A typical gate path for the pick-and-place operation of the new hybrid robot is shown in Fig. 15, in which there are twelve key path points from  $Q_1$  to  $Q_{12}$ , and eleven sub-paths. The motion trajectory equation of each sub-path has been assigned in Table 2 for a given period of motion  $T$  with respect to frame 0.

Taking  $T = 2$  s for example, based on the inverse kinematic model of the new robot in Section 3, angles and angular velocities of the

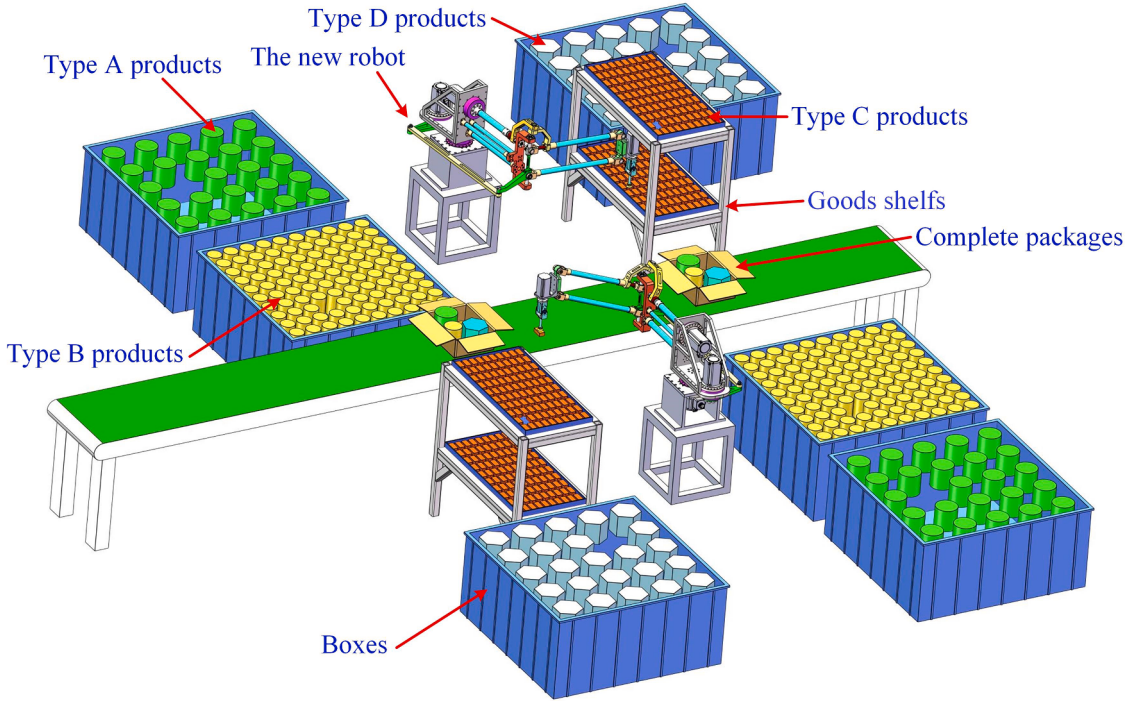


**Fig. 19.** Schematic diagram of disassembly and sorting applications in a warehouse.

four actuation joints can be computed for the given output trajectories. The simulative results of angles and angular velocities of the four actuation joints can be also obtained based on the virtual prototype. Fig. 16 shows the comparisons of those results, in which  $\theta_i$ ,  $\dot{\theta}_i$  and  $\ddot{\theta}_i$  represent computational angles, simulative angles, computational angular velocity, and simulative angular velocity of the  $i$ th actuation joint. The comparisons show that the computational results and simulative results are consistent, which verifies the correctness of the established kinematic model.

Through reading actuator data from joint encoders, experimental angles and angular velocities of four actuation joints can be obtained. Fig. 17 shows the comparisons between computational results and experimental results, in which  $\theta_{i+}$  and  $\dot{\theta}_{i+}$  represent experimental angles and experimental angular velocity of the  $i$ th actuation joint. The comparisons show that two kinds of results are consistent, with only small errors which are brought by manufacture and assembly of the robot.

Load joint values of Fig. 16 to the physical prototype, the experimental output path of the robot can be obtained. Fig. 18 shows the end-effector positions of the robot when  $t = 0$  s,  $5/8$  s,  $7/4$  s and 2 s. It can be seen that the experimental output path is consistent with the theoretical path shown in Fig. 18. Based on the above consistency between theoretical results and experimental results, the design and modeling of the robot can be verified to be effective.

## 6. Discussion

The new robot is expected to apply to small loads in large workspace, for example, the robotic broken-case piece picking application [26–28] in a warehouse, as shown in Fig. 19, in which a robot is expected to be used to pick and place different types of products from goods shelf and boxes into packages. In such an application, efficiency is very important, so a robot with large workspace and high speed is expected, which is just one of the motivations of the paper.

Compared with the SCARA robot with large translation along Z axis, the proposed robot has smaller inertia in Z axis direction, has a lower self height and self weight, and contains no prismatic pair with a relatively short service life [3,29].

For the Broken-case Piece Picking application, kinematic control is enough to satisfy operation requirements. Hence, we present the mechanism design, position analysis, velocity analysis, acceleration analysis, workspace analysis and prototype experiment of the new robot. We intend to perform other performance analyses such as stiffness and dynamics analysis in further works. Besides, lightweight design, gravity compensation, and dimensional optimized design will be considered in our further work to reduce its inertia as much as possible.

## 7. Conclusions

A novel 4-DOF hybrid robot (named Hybrid-Long-Scara robot) combining the advantages of parallel robots and serial robots is developed in this paper. The new robot only includes revolute pairs and its most actuators are located at the base or close to the base to

obtain high-speed motion. The closed-form displacement and velocity models of the new robot are established and its workspace is quantitatively analyzed. The virtual and physical prototypes of the Hybrid-Long-Scara robot are developed to illustrate the correctness of the mechanical design and the kinematic model. Different from typical Scara robots and palletizing robots, the Hybrid-Long-Scara robot can obtain larger vertical workspace based on a compact structure, can realize pick and place tasks inside a goods shelf, and occupy low vertical installation space. With these characteristics, the new robot has a good application prospect in the industry.

### CRediT authorship contribution statement

**Wen-ao Cao:** Writing – original draft, Project administration, Methodology. **Shiwei Li:** Visualization, Software, Investigation. **Peng Cheng:** Writing – review & editing, Visualization, Methodology, Investigation. **Mingfeng Ge:** Software, Investigation. **Huafeng Ding:** Resources, Project administration, Conceptualization. **Jingpei Lai:** Visualization, Software.

### Declaration of competing interest

The authors declare that they have no known competing financial interests or personal relationships that could have appeared to influence the work reported in this paper.

### Data availability

The authors are unable or have chosen not to specify which data has been used.

### Acknowledgment

This work was funded by the National Natural Science Foundation of China (No. 51875538), and by the Knowledge Innovation Program of Wuhan-Basic Research (No. 2022010801010198).

### References

- [1] J. Gallardo, R. Lesso, J.M. Rico, G. Alici, The kinematics of modular spatial hyper-redundant manipulators formed from RPS-type limbs, *Rob. Auton. Syst.* 59 (2011) 12–21.
- [2] M. Isaksson, T. Brogardh, S. Nahavandi, Parallel manipulators with a rotation-symmetric arm system, *J. Mech. Des. Trans. ASME* 134 (2012) 114503.
- [3] F. Pierrot, V. Nabat, O. Company, S. Krut, P. Poignet, Optimal design of a 4-DOF parallel manipulator: from academia to industry, *IEEE Trans. Rob.* 25 (2009) 213–224.
- [4] S. Briot, I.A. Bonev, Pantopteron-4: a new 3T1R decoupled parallel manipulator for pick-and-place applications, *Mech. Mach. Theory* 45 (2010) 707–721.
- [5] O. Salgado, O. Altuzarra, E. Amezua, A. Hernández, A parallelogram-based parallel manipulator for Schönhflies motion, *J. Mech. Des.* 129 (2006) 1243–1250.
- [6] Z. Huang, Q. Li, Type synthesis of symmetrical lowermobility parallel mechanisms using the constraint synthesis method, *Int. J. Rob. Res.* 22 (2003) 59–72.
- [7] B. Hu, J. Yu, Unified solving inverse dynamics of 6-DOF serial-parallel manipulators, *Appl. Math. Model.* 39 (2015) 4715–4732.
- [8] B. Hu, Z. Liu, J. Zhao, J. Zhao, J. Yao, Kinematics analysis of 6-degrees-of-freedom parallel + serial type hybrid mechanisms containing parallel mechanism with high coupling motions, *J. Mech. Rob.* 16 (2023) 024501.
- [9] N. Shen, H. Yuan, J. Li, Z. Wang, N. Lu, Y. Lu, Dynamic modeling and simulation of a hybrid robot, *J. Mech. Rob.* 15 (2022) 011012.
- [10] K. Neumann, Tricept application, in: 3rd Chemnitz Parallel Kinematic Seminar, 2002, pp. 547–551.
- [11] L. Romdhane, Design and analysis of a hybrid serial-parallel manipulator, *Mech. Mach. Theory* 34 (1999) 1037–1055.
- [12] L.-W. Tsai, S. Joshi, Kinematic analysis of 3-DOF position mechanisms for use in hybrid kinematic machines, *J. Mech. Des. Trans. ASME* 124 (2002) 245–253.
- [13] T. Huang, M. Li, X.M. Zhao, J.P. Mei, D.G. Chetwynd, S.J. Hu, Conceptual design and dimensional synthesis for a 3-DOF module of the TriVariant - A novel 5-DOF reconfigurable hybrid robot, *IEEE Trans. Rob.* 21 (2005) 449–456.
- [14] C. Liang, M. Ceccarelli, Design and simulation of a waist-trunk system for a humanoid robot, *Mech. Mach. Theory* 53 (2012) 50–65.
- [15] D. Zhao, C. Dong, H. Guo, W. Tian, Kinematic calibration based on the multicollinearity diagnosis of a 6-DOF polishing hybrid robot using a laser tracker, *Math. Probl. Eng.* 2018 (2018) 5602397.
- [16] X. Wang, J. Wu, Y. Wang, Dynamics evaluation of 2UPU/SP parallel mechanism for a 5-DOF hybrid robot considering gravity, *Rob. Auton. Syst.* 135 (2021) 103675.
- [17] Y. Wu, Z. Yang, Z. Fu, J. Fei, H. Zheng, Kinematics and dynamics analysis of a novel five-degrees-of-freedom hybrid robot, *Int. J. Adv. Rob. Syst.* 14 (2017) 1–8.
- [18] J. Li, F. Ye, N. Shen, Z. Wang, L. Geng, Dimensional synthesis of a 5-DOF hybrid robot, *Mech. Mach. Theory* 150 (2020) 103865.
- [19] C. Dong, H. Liu, J. Xiao, T. Huang, Dynamic modeling and design of a 5-DOF hybrid robot for machining, *Mech. Mach. Theory* 165 (2021) 104438.
- [20] C. Qi, D. Li, Y. Hu, F. Gao, W. Wang, W. Ma, Stability analysis and distortion compensation of robot structure dynamics for a hybrid simulator, *J. Mech. Des.* 145 (2023) 073302.
- [21] Y. Tao, F. Chen, H. Xiong, Kinematics and workspace of a 4-DOF hybrid palletizing robot, *Adv. Mech. Eng.* 6 (2015) 1–6.
- [22] C. Zhao, H. Guo, R. Liu, Z. Deng, B. Li, J. Tian, Actuation distribution and workspace analysis of a novel 3(3RRIS) metamorphic serial-parallel manipulator for grasping space non-cooperative targets, *Mech. Mach. Theory* 139 (2019) 424–442.
- [23] H. Yu, Q. Sun, C. Wang, Y. Zhao, Frequency response analysis of heavy-load palletizing robot considering elastic deformation, *Sci. Prog.* 103 (2020) 1–10.
- [24] B. Hu, Y. Huo, J. Gao, D. Zhang, CGA-based approach for the inverse displacement of serial-parallel manipulators, *Mech. Mach. Theory* 176 (2022) 105011.
- [25] J. Wang, Y. Zhang, X. Liu, Control system of 4-DOF palletizing robot based on improved R control multi-objective trajectory planning, *Adv. Mech. Eng.* 13 (2021) 1–7.
- [26] D.B. Đurđević, M.D. Miljuša, Piece picking technology selection, in: Proceedings of the 4th Logistics International conference, 2019, pp. 263–273. Belgrade, Serbia.
- [27] N. Kimura, R. Sakai, S. Katsumata, N. Chihara, Simultaneously determining target object and transport velocity for manipulator and moving vehicle in piece-picking operation, in: 2019 IEEE 15th International Conference on Automation Science and Engineering (CASE), IEEE, 2019, pp. 1066–1073.
- [28] N. Boysen, D. Briskorn, S. Emde, Parts-to-picker based order processing in a rack-moving mobile robots environment, *Eur. J. Oper. Res.* 262 (2017) 550–562.
- [29] Y. Li, Y. Ma, S. Liu, Z. Luo, J. Mei, T. Huang, D. Chetwynd, Integrated design of a 4-DOF high-speed pick-and-place parallel robot, *CIRP Ann.* 63 (2014) 185–188.